ATLAS CONF Note

ATLAS-CONF-2023-070

26th September 2023

Search for pair-production of vector-like quarks in lepton+jets final states containing at least one b-jet using the Run 2 data from the ATLAS experiment

The ATLAS Collaboration

A search is presented for the pair-production of heavy vector-like quarks in the lepton+jets final state using 140 fb^{-1} of proton–proton collision data with $\sqrt{s}$ = 13 TeV collected with the ATLAS detector. The search is optimised for vector-like top quarks (T) that decay into a W boson and a b quark, with one W boson decaying leptonically and the other hadronically, though other vector-like quark flavours and decay modes are considered. Events are selected with one high transverse-momentum electron or muon, large missing transverse momentum, a large-radius jet identified as a W boson, and multiple small-radius jets, at least one of which is b-tagged. Vector-like T quarks with 100% branching ratio to Wb are excluded for masses below 1700 GeV. These limits can also be applied to vector-like Y quarks which decay exclusively to a W boson and a b quark. Isospin singlets with $\mathcal{B}(T \to Wb : Ht : Zt) = 1/2 : 1/4 : 1/4$ are excluded for masses below 1420 GeV.

ATLAS-CONF-2023-070
24 October 2023

1 Introduction

The Standard Model (SM) of particle physics has been extremely successful in describing elementary particles and their interactions, yet its many shortcomings reveal that it is incomplete. In particular, naturalness [1] suggests that a more complete theory will provide an explanation for how radiative divergences to the Higgs boson mass from t-quark loops are cancelled. Extensions of the SM, such as extra dimensions [2], composite Higgs [3, 4] and Little Higgs [5] models, predict the existence of vector-like quarks (VLQs) that could mitigate these large radiative corrections to the Higgs boson mass. The VLQs are spin-1/2, colour-triplets that have the same weak isospin for left- and right-handed chiralities. Thus, VLQs would not acquire mass via the Higgs boson [6], allowing them to evade the limits that exclude additional SM-like quarks [7]. To cancel the Higgs mass divergence from top-quark loops, the VLQs must couple preferentially to third-generation quarks, but could be SU(2) singlets, doublets, or triplets of T, B, X or Y; where T and B have the same electric charge as the SM t and b quarks, while the Y and X have a charge of $-4/3$ and $5/3$. In the simplest models, the mass difference between VLQs in a given SU(2) multiplet must be small to satisfy constraints from precision electroweak measurements [6], excluding cascading decays such as $T \to WB \to WWt$. The VLQs are able to decay via a flavor-changing neutral current or a charged current, allowing the T and B to each have three possible decays: $T \to Wb/Zt/Ht$ and $B \to Wt/Zb/Hb$. With no SM partner to the Y or X, these can only decay via $Y \to Wb$ and $X \to Wt$. Decays to final states with first and second generation quarks, though not forbidden, are not favored as they would not address the hierarchy problem. Examples of a Feynman diagram for T and B pair production and decay are shown in Figure 1.

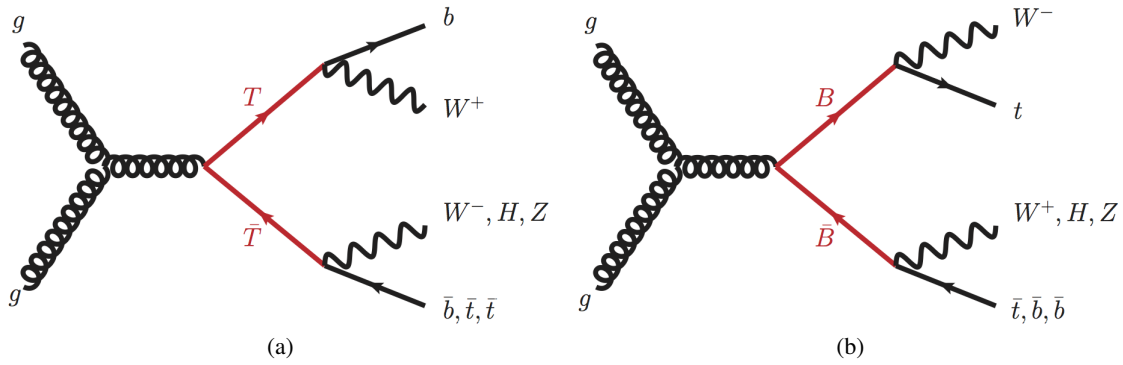

Figure 1: Representative tree-level Feynman diagrams for (a) $T\bar{T}$ and (b) $B\bar{B}$ production for which at least one of the VLQs decays via a W boson.

The branching ratio of the VLQ decay to Standard Model particles is not fixed by the theory, therefore, all possible VLQ decays and branching ratios need to be probed in searches for VLQs using data from the ATLAS or CMS experiments. A combination of searches for pair-production of VLQs by ATLAS using 36 fb^{-1} of data from Run 2 excludes VLQs with masses below 1310 GeV for any branching ratio [8]. ATLAS searches for pair-produced VLQs using the full proton-proton collision dataset collected during Run 2 of the Large Hadron Collider (LHC) include a search in final states with one lepton, jets and large missing transverse energy [9], mostly sensitive to the decay $T \to Zt$ or $B \to Wt$ and in final states with at least one leptonically decaying Z boson and a third-generation quark [10], which is mainly sensitive to $T \to Zt$ and $B \to Zb$. Singly produced VLQs have also been searched for by ATLAS using the full LHC Run 2 dataset [11, 12], but the interpretation [13] of the search results depends on an additional constant

for the coupling to electroweak bosons. CMS published searches for pair production [14] and single production [15–17] of vector-like quarks using 137 fb^{-1} of data taken during the LHC Run-2. ATLAS has previously performed a search for pair-produced vector-like quarks in the one lepton+jets final state using 36 fb^{-1} of Run 2 data collected at the LHC from 2015 to 2016 and optimized to the $T \to Wb$ decay [18]. That search excluded T quarks masses below 1350 GeV in the scenario $\mathcal{B}(T \to Wb) = 1$. A recent search for pair-produced vector-like quarks by CMS in leptonic final states using the full CMS Run 2 dataset of 138 fb^{-1} excludes the scenario $\mathcal{B}(T \to Wb) = 1$ for masses below 1540 GeV [19].

This paper presents a search for the pair production of VLQs decaying into third-generation quarks using the proton-proton collision data collected at the LHC from 2015 to 2018 at a centre-of-mass energy of 13 TeV with the ATLAS experiment, increasing the data set with respect to the previous search in this decay channel from 36 fb^{-1} to 140 fb^{-1}. The analysis is optimised for the $T\bar{T} \to WbW\bar{b}$ channel with one W decaying leptonically and the other hadronically, resulting into a final state with exactly one lepton, missing transverse momentum and jets, but the search is also sensitive to the other VLQs and decay modes. Targeting events with a leptonically decaying W ($W \to \ell\nu$ with $\ell = e, \mu$) suppresses SM processes with purely hadronic final states, while the hadronically decaying W provides a large branching ratio. Vector-like T candidates are reconstructed such that the mass difference between the leptonically and hadronically decaying T candidates is minimised. The reconstructed mass of the leptonically decaying T is then used as the discriminating variable to test for the presence of a VLQ signal. The dominant background processes are $t\bar{t}$, W+jets, and single-top-quark production. Control regions enhanced in $t\bar{t}$ or W+jets events are used to correct the mismodelling observed in Monte-Carlo (MC) simulations of those processes. Finally, a profile likelihood fit is performed on the measured distributions as a function of VLQ masses and decay branching ratios to test for the presence of VLQ signals.

2 ATLAS detector

The ATLAS experiment [20] at the LHC is a multipurpose particle detector with a forward–backward symmetric cylindrical geometry and a near 4π coverage in solid angle.[1] It consists of an inner tracking detector (ID) surrounded by a thin superconducting solenoid providing a 2 T axial magnetic field, electromagnetic and hadron calorimeters, and a muon spectrometer. The inner tracking detector covers the pseudorapidity range $|\eta| < 2.5$. It consists of silicon pixel, silicon microstrip, and transition radiation tracking detectors. Lead/liquid-argon (LAr) sampling calorimeters provide electromagnetic (EM) energy measurements with high granularity. A steel/scintillator-tile hadron calorimeter covers the central pseudorapidity range ($|\eta| < 1.7$). The endcap and forward regions are instrumented with LAr calorimeters for both the EM and hadronic energy measurements up to $|\eta| = 4.9$. The muon spectrometer (MS) surrounds the calorimeters and is based on three large superconducting air-core toroidal magnets with eight coils each. The field integral of the toroids ranges between 2.0 and 6.0 T m across most of the detector. The muon spectrometer includes a system of precision tracking chambers and fast detectors for triggering. A two-level trigger system is used to select events. The first-level trigger is implemented in hardware and uses a subset of the detector information to accept events at a rate below 100 kHz. This is followed by a software-based trigger that reduces the accepted event rate to 1 kHz on average depending on the data-taking conditions. An extensive software suite [21] is used in data simulation, in the reconstruction

[1] ATLAS uses a right-handed coordinate system with its origin at the nominal interaction point (IP) in the centre of the detector and the z-axis along the beam pipe. The x-axis points from the IP to the centre of the LHC ring, and the y-axis points upwards. Polar coordinates (r, ϕ) are used in the transverse plane, ϕ being the azimuthal angle around the z-axis. The pseudorapidity is defined in terms of the polar angle θ as $\eta = -\ln\tan(\theta/2)$. Angular distance is measured in units of $\Delta R \equiv \sqrt{(\Delta\eta)^2 + (\Delta\phi)^2}$.

and analysis of real and simulated data, in detector operations, and in the trigger and data acquisition systems of the experiment.

3 Data and simulated event samples

The results presented in this search use data from pp collisions with a centre-of-mass energy of $\sqrt{s} = 13$ TeV. The data were collected between 2015 and 2018 with the ATLAS detector, corresponding to an integrated luminosity of 140 fb^{-1} [22, 23]. A set of single-electron [24] and single-muon triggers [25] were used, with transverse momentum (p_{T}) lowest thresholds in the range 20–26 GeV depending on the lepton flavour and data-taking period. In addition, data were recorded using a trigger targeting events with large missing transverse energy ($E_{\mathrm{T}}^{\mathrm{miss}}$) with thresholds of 70, 90 or 110 GeV, depending on the data taking period. All detector subsystems are required to have been operational during data taking and to fulfill data quality requirements [26].

Signal events and SM background with at least one prompt lepton are modelled by MC simulation. Contributions from processes surviving selection requirements due to non-prompt leptons or hadronic jets misidentified as leptons (dominated by QCD multijet events) are estimated using a data-driven method, with MC samples serving as cross checks. All samples were produced using the ATLAS simulation infrastructure [27] and GEANT4 [28]. For the estimation of some systematic uncertainties, a faster detector simulation employing a parameterisation of the calorimeter response was used [29]. Unless specified otherwise, the parton shower, hadronisation, and underlying events are modelled using PYTHIA8.230 [30], with parameters set according to the A14 set of tunable parameters (the A14 "tune") [31] and using the NNPDF2.3LO set of parton distribution functions (PDFs) [32]. The effect of additional pp interactions per bunch crossing (pile-up) is accounted for by overlaying the hard-scattering process with minimum-bias events generated with PYTHIA 8.186 [33] using the A3 tune [34] and NNPDF2.3LO PDFs. Different pile-up conditions between data and MC are taken into account by reweighting the mean number of interactions per bunch crossing in MC to the number observed in data.

Signal events for the production and decay of $T\bar{T}$ and $B\bar{B}$ were generated at leading order using PROTOS v.2.2 [35] with VLQ masses from 1000 GeV to 2 TeV in steps of 100 GeV for 1000-1800 GeV and in steps of 200 GeV elsewhere. The samples were produced for the singlet model, with alternative branching ratio scenarios obtained by reweighting the events based on the decay mode. Samples for the doublet model with a mass of 1.2 TeV were also produced to confirm that kinematic differences due to isospin have negligible impact on the results. The signal cross sections were calculated with TOP++ 2.0 [36] at next-to-next-to-leading order (NNLO) in QCD including the resummation of next-to-next-to-leading logarithmic (NNLL) soft-gluon terms.

The dominant background arises from the production of t-quark pairs ($t\bar{t}$). Events with a single t-quark (single top) or a W boson and jets (W+jets) also make significant contributions. Finally, events containing a Z boson and jets (Z+jets), three or four t-quarks, multi-boson events, and t-quark pairs produced in association with heavy bosons also have small contributions.

The production of $t\bar{t}$ events is modelled using the POWHEG BOX v2 [37–40] generator at NLO precision in QCD with the NNPDF3.0NLO [41] PDFs and the h_{damp} parameter[2] set to $1.5m_t$ [42]. The dependence on parton shower and hadronisation models is evaluated by comparing the nominal $t\bar{t}$ sample with an alternate

[2] The h_{damp} parameter is a resummation damping factor and one of the parameters that controls the matching of POWHEG matrix elements (ME) to the parton shower and thus effectively regulates the high-p_{T} radiation against which the $t\bar{t}$ system recoils.

sample produced via the POWHEG BOX v2 generator using the NNPDF3.0NLO PDFs and interfaced with HERWIG7.04 [43, 44] using the MMHT2014LO PDFs [45] and the H7UE tune [44]. An uncertainty in the matching of the NLO matrix elements (ME) to the parton shower is assessed by comparing the nominal sample to one generated with MADGRAPH5_AMC@NLO 2.6.0 [46] using the NNPDF3.0NLO PDFs. The impact of a potential under-estimation of the initial state radiation (ISR) is evaluated by comparing the nominal sample to one produced with h_{damp} increased to $3m_t$, the renormalisation and factorisation scales divided by two, and using the "Var3cUp" weight of the A14 tune. The impact of a potential over-estimation of the ISR is evaluated by comparing the nominal sample to one obtained by doubling the renormalisation and factorisation scales and choosing the "Var3cDown" weight of the A14 tune [47]. The impact of the uncertainty in the modeling of final state radiation (FSR) is evaluated by doubling or halving the renormalisation scale for emissions from the parton shower.

The associated production of a t-quark with a W boson is hypothesised to account for the vast majority of single top events. These events were modelled by the POWHEG BOX v2 generator at NLO in QCD using the five-flavour scheme and the NNPDF3.0NLO PDFs. The nominal sample uses the diagram removal (DR) scheme [48] to remove the contribution from Feynman diagrams already included in the $t\bar{t}$ production. An alternative sample generated using the diagram subtraction scheme (DS) [42, 48] is used to evaluate an uncertainty due to the choice of $t\bar{t}/Wt$ overlap removal scheme. The uncertainty due to the parton shower and hadronisation models is evaluated by comparing the nominal sample of events with events generated by the POWHEG BOX v2 generator interfaced to HERWIG7.04 using the H7UE tune and the MMHT2014LO PDFs. To assess the uncertainty in the matching of the ME to the parton shower, the nominal tW sample is compared to a sample generated with the MADGRAPH5_AMC@NLO 2.6.2 generator at NLO in QCD using the five-flavour scheme and the NNPDF2.3LO PDFs [41].

The small contributions from single top quark t-channel and s-channel production were modelled using the POWHEG BOX v2 [38–40, 49, 50] generator at NLO in QCD using the four-flavour scheme (t-channel) or the five-flavour scheme (s-channel) and the NNPDF3.0NLO PDFs. The uncertainty due to the parton shower and hadronisation models is evaluated by comparing the nominal sample of events with events generated by the POWHEG BOX v2 generator at NLO precision in QCD using the five-flavour scheme and interfaced to HERWIG7.04 using the H7UE tune and the MMHT2014LO PDFs. To assess the uncertainty in the matching of NLO precision ME to the parton shower, the nominal sample is compared to a sample generated with the MADGRAPH5_AMC@NLO 2.6.2 generator at NLO precision in QCD using the five-flavour scheme and NNPDF2.3NLO or NNPDF3.0NLO PDFs for the t- and s-channel, respectively.

The production of V+jets ($V = W, Z$) was simulated with the SHERPA2.2.1 [51] generator using NLO ME for up to two partons, and LO precision ME for up to four partons calculated with the Comix [52] and OPENLOOPS [53–55] libraries. They were matched with the SHERPA parton shower [56] using the MEPS@NLO prescription [57–60] using the tune developed by the SHERPA authors. The NNPDF3.0NNLO set of PDFs was used and the samples are normalised to a NNLO prediction [61]. Samples of diboson events (VV) were simulated with the SHERPA2.2.1 or 2.2.2 [51] generator at NLO accuracy in QCD for up to one additional parton and at LO accuracy for up to three additional parton emissions, including off-shell effects and H boson contributions, where appropriate. The ME calculations were matched and merged with the SHERPA parton shower based on Catani–Seymour dipole factorisation [52, 56] using the MEPS@NLO prescription. The virtual QCD corrections were provided by the OPENLOOPS library [53–55]. The NNPDF3.0NNLO set of PDFs was used, along with the dedicated tune developed by the SHERPA authors.

The production of $t\bar{t}V$ events is modelled using the MADGRAPH5_AMC@NLO 2.3.3 generator at NLO with the NNPDF3.0NLO PDF and PYTHIA8.210 with the A14 tune and the NNPDF2.3LO PDFs for the

parton shower and hadronisation. The production of $t\bar{t}H$ events is modelled using the POWHEG BOX v2 generator at NLO with the NNPDF3.0NLO PDF set. The production of tWZ events is modelled using the MADGRAPH5_AMC@NLO 2.3.3 generator at NLO with the NNPDF3.0NLO PDF and PYTHIA8.211 with the A14 tune and the NNPDF2.3LO PDF set for the parton shower and hadronisation. The diagram removal scheme described in Ref. [48] was employed to handle the overlap between tWZ and $t\bar{t}Z$, and was applied to the tWZ sample. The small contributions from tZ, three and four t-quarks events, and $t\bar{t}WW$ events were simulated with MADGRAPH5_AMC@NLO 2.2.2 interfaced to PYTHIA8.186 using the A14 tune. The small contributions from processes from $t\bar{t}H$, tWZ, tZ, $ttWW$ and multi-top production is summarised as "rare top" processes. Multijet MC samples were generated using the SHERPA 2.1.1 generator. The matrix element calculation was included for the $2 \rightarrow 2$ process at leading order, and the default SHERPA parton shower based on Catani–Seymour dipole factorisation was used for the showering with p_{T} ordering, using the CT10 PDF set [62].

Decays of b- and c-hadrons were handled by EVTGEN 1.6.0 [63] in all simulations except SHERPA, for which the default SHERPA configuration recommended by the SHERPA authors was used.

4 Object reconstruction

Electrons are reconstructed [64] from clusters in the EM calorimeter matched with ID tracks. Electron candidates must be in the central region of the detector ($|\eta| < 2.47$) with $p_{\mathrm{T}} > 27$ GeV and match a track with $|z_0 \sin\theta| < 0.5$ mm and $\left|d_0/\sigma_{d_0}\right| < 5$; where d_0 is the impact parameter between the track and hard scatter vertex and z_0 is the minimum distance in z between the track and primary vertex. Any candidates in the transition region between the barrel and endcap calorimeters ($1.37 < |\eta| < 1.52$) are removed. "Baseline electrons" must fulfill the *medium likelihood* identification criteria [64], with no selection on the isolation. "Tight electrons" must fulfill the *tight likelihood* identification criteria, plus the following isolation requirements in both the calorimeter and the ID [64]. The first isolation requirement is $E^{\mathrm{isol}}_{\mathrm{T,\,cone}}/p^{e}_{\mathrm{T}} < 0.2$; where p^{e}_{T} is the electron candidate p_{T} and $E^{\mathrm{isol}}_{\mathrm{T,cone}}$ is the energy deposited in the calorimeter in a radius $\Delta R = 0.2$ with the candidate direction; any leakage energy and energy from pile-up are subtracted. The second is $p^{\mathrm{isol}}_{\mathrm{T,var}}/p^{e}_{\mathrm{T}} < 0.15$; where $p^{\mathrm{isol}}_{\mathrm{T,var}}$ is the sum of the track p_{T} without the electron candidate in a cone of radius $\Delta R = \min(10\,\mathrm{GeV}/p^{e}_{\mathrm{T}}, 0.2)$. Scale factors are used to correct for differences in reconstruction, identification, isolation and trigger selection efficiencies between data and simulation [64].

Muons are reconstructed [65] from combined tracks in the MS and the ID, with "baseline muons" required to pass the *loose* identification criteria and no selection on the isolation, while "tight muons" must fulfill *tight* identification criteria [66] and satisfy the track-based isolation requirements defined by the *TightTrackOnly* working point. This working point uses the scalar sum of the p_{T} of all tracks that are within a cone of size $\Delta R = \min(0.3, 10\,\mathrm{GeV}/p^{\mu}_{\mathrm{T}})$ around the muon candidate, where p^{μ}_{T} is the candidate muon p_{T}. The track associated with the muon candidate under consideration is excluded from the sum. The muon is selected if this sum is less than 6% of p^{μ}_{T}. Finally, all muon candidates are required to have $|z_0 \cdot \sin\theta| < 0.5$ mm and a d_0 significance smaller than 3. Muons are calibrated [67] and are required to have $p_{\mathrm{T}} > 15$ GeV and to be reconstructed within $|\eta| < 2.5$. Efficiency scale factors are used to correct for differences in muon reconstruction, identification, vertex association, isolation and trigger efficiencies between simulation and data [66].

Small-radius (small-R) jet candidates are built from particle-flow objects [68, 69], using the anti-k_t algorithm [70, 71] with a radius parameter of $R = 0.4$. The particle-flow algorithm combines information

about tracks in the ID and energy deposits in the calorimeters to form the input for the jet reconstruction. The jet energy is calibrated to the particle scale by using a sequence of corrections, including simulation-based corrections and in situ calibrations [69]. Jets are required to have $p_{\mathrm{T}} > 25\,\mathrm{GeV}$ and $|\eta| < 2.5$. To reject jets originating from pile-up interactions, jet candidates with $|\eta| < 2.4$ and $p_{\mathrm{T}} < 60\,\mathrm{GeV}$ are required to satisfy the 'tight' jet vertex tagger (JVT) criterion [72]. An algorithm based on deep and recurrent neural networks, called DL1r, is used to identify small-R jets containing a b-hadron decay [73]. Jets are considered to be b-tagged if they pass the criteria for the operating point with an efficiency of 77 % and mistag rates for charm and light jets of 17.7% and 0.52%, respectively, as determined in simulated $t\bar{t}$ events [74]. The b-tagging efficiencies in simulation, as well as the charm and light mistag rates, are corrected to match the efficiencies in data [75, 76].

An overlap removal procedure is applied to prevent double counting of ambiguous reconstructed objects, using the baseline lepton definitions. First, electron–muon overlap is handled by removing muons sharing a track in the ID with an electron if the muon is calorimeter-tagged, and otherwise removing the electron. Subsequently, overlap between jets and leptons is removed by rejecting any jets within $\Delta R = 0.2$ of an electron and afterwards rejecting any electrons within $\Delta R = 0.4$ of a jet. Similarly, jets are discarded if they have fewer than three associated tracks and are within $\Delta R = 0.2$ of a muon candidate. Otherwise, the muon is rejected if it lies within $\Delta R = \min(0.4, 0.04 + 10\,\mathrm{GeV}/p_{\mathrm{T}}^{\mu})$ of a jet.

The missing transverse momentum, with magnitude $E_{\mathrm{T}}^{\mathrm{miss}}$, is defined as the negative vectorial sum of the transverse momenta of all calibrated objects in an event, plus a track-based soft-term which takes into account energy depositions associated with the primary vertex but not with any calibrated object [77].

Finally, large-radius (large-R) jets are constructed from the noise-suppressed topological calorimeter-cell clusters calibrated using local hadronic cell reweighting [78] using the anti-k_t algorithm with $R = 1.0$. To reduce the impact of soft radiation, a grooming algorithm called "trimming" [79] is applied. Constituent small-R jets, reclustered with the k_t algorithm with a radius parameter $R = 0.2$, with p_{T} less than 5% of the large-R jet p_{T} are removed. The large-R jets are required to have $p_{\mathrm{T}} > 200\,\mathrm{GeV}$, $|\eta| < 2.0$ and a mass larger than 50 GeV. The jet energy scale (JES) and resolution (JER) and the mass scale (JMS) and resolution (JMR) of large-radius jets are calibrated [80, 81]. A W-tagging algorithm identifies high-p_{T} hadronically decaying W bosons, whose decay products are collimated to a single large-radius jet [82], with an efficiency of 80%. The W-tagging algorithm applies criteria on the mass of the large-radius jet, the number of inner-detector tracks associated with the jets and the D_2 variable [82, 83]. Calibration factors correct the W-tagging efficiency in simulation to the efficiency in data [84].

5 Event selection and reconstruction

This search targets final states with exactly one electron or muon, missing transverse momentum, and jets. Events are either required to be selected by the lowest un-prescaled single electron or muon trigger, or a trigger targeting events with large $E_{\mathrm{T}}^{\mathrm{miss}}$, as described in Section 3. If the event is selected by a single lepton trigger, the selected lepton must have $p_{\mathrm{T}} > 27\,\mathrm{GeV}$ and be matched to the object that triggered the event. If the event is selected by the $E_{\mathrm{T}}^{\mathrm{miss}}$ trigger, it must have $E_{\mathrm{T}}^{\mathrm{miss}} > 200\,\mathrm{GeV}$. The $E_{\mathrm{T}}^{\mathrm{miss}}$ trigger selection has been added in order to compensate for the efficiency loss of the single muon triggers at high muon p_T.

Events are required to have exactly one tight muon with $p_{\mathrm{T}} > 27\,\mathrm{GeV}$ or one tight electron with $p_{\mathrm{T}} > 60\,\mathrm{GeV}$. Increasing the p_{T} threshold for electrons to $p_{\mathrm{T}} > 60\,\mathrm{GeV}$ facilitates the estimation of the background from non-prompt electrons. The fake lepton background estimation relies on the difference between the

efficiency that a fake lepton passes only the baseline lepton selection and the efficiency that it passes as well the tight lepton criteria. The single electron trigger selection, which is part of both the baseline and tight electron selection, however, imposes very strict selections on the electrons with $p_{\mathrm{T}} < 60\,\mathrm{GeV}$ already, making it difficult to define a selection tighter than the baseline electron criteria. Studies showed that increasing the electron p_{T} threshold to 60 GeV does not impact the analysis sensitivity. Events with additional leptons with $p_{\mathrm{T}} > 25\,\mathrm{GeV}$ satisfying the baseline criteria are vetoed. In addition, all events must have $E_{\mathrm{T}}^{\mathrm{miss}} > 60\,\mathrm{GeV}$ and contain at least three small-R jets, at least one of which must be b-tagged. The criteria described above is referred to as "pre-selection".

This search focuses on T quarks with mass above the previous limit, 1.35 TeV [18]. The large mass of the T will lead to decay products with large p_{T}, which in turn will have collimated decay products. In particular, the hadronically decaying W boson will produce a large-R jet, so events are required to contain at least one W-tagged large-R jet. If more than one large-R jet is W-tagged, the one with a mass closest to the W-boson mass ($m_W = 80.38\,\mathrm{GeV}$) is selected as the hadronically decaying W boson (W_{had}) for reconstructing the two T candidates. The leptonically decaying W boson (W_{lep}) is reconstructed from the system of the selected lepton and reconstructed neutrino. The p_{T} of the reconstructed neutrino is determined from the $E_{\mathrm{T}}^{\mathrm{miss}}$ and the p_z is calculated by interpreting the lepton-neutrino system has an invariant mass of m_W. When two real solutions are obtained, the one with the smaller absolute value is used. When the solutions are complex, a real solution is obtained by adjusting the components of the neutrino momenta to minimise a χ^2 parameter that takes into account the uncertainties on the neutrino and lepton momenta and W-boson mass. Finally, the angular distance between the lepton and the reconstructed neutrino is required to be $\Delta R(\ell, \nu) < 0.7$.

Reconstruction of the two T candidates is done by pairing each of the W candidates, W_{lep} and W_{had}, with a small-R jet. The small-R jets are selected for pairing with the W-boson candidates by minimising the difference in the hadronic and leptonic reconstructed T masses, $\Delta m_{\mathrm{VLQ}} \equiv |m_T^{\mathrm{lep}} - m_T^{\mathrm{had}}|$.

If the event contains one b-tagged jet, only combinations that include the b-tagged jet are considered. If the event contains two or more b-tagged jets, only combinations with the two b-tagged jets leading in p_{T} are considered. Signal events are expected to have VLQs with low p_{T} and high mass, causing the jet paired with the W_{had}, referred to as b_{had}, to be well separated from the W_{had}. By contrast, $t\bar{t}$ events will have high-p_{T} t-quarks that lead to a small opening angle between the resulting W and b. Therefore, a requirement of $\Delta R(W_{\mathrm{had}}, b_{\mathrm{had}}) > 1.0$ is imposed to reduce the $t\bar{t}$ background. Well reconstructed signal events should also have small values of Δm_{VLQ}, with both reconstructed T masses m_T^{lep} and m_T^{had} close to the actual mass of the T. A similar statement can be made for $t\bar{t}$ events, but the reconstructed variables m_T^{lep} and m_T^{had} will be close to the top quark mass m_t. Production of $T\bar{T}$ events with other decays, such as $T \to Ht/Zt$, will tend to have m_T^{lep} and m_T^{had} near the T mass, but with large values of Δm_{VLQ} as the VLQ reconstruction is less adapted to t quarks from the T decay. Detector effects, final state radiation, and mis-reconstruction can also broaden the reconstructed mass peaks for signal and $t\bar{t}$ events. In contrast, a smooth distribution in Δm_{VLQ} is expected for background processes, such as W+jets and single top. The variable Δm_{VLQ} is therefore used to separate regions enriched in single top background with similar kinematic properties as the single top events in the signal region.

The scalar sum S_{T} of the p_{T} of the selected small-R jets, the lepton and the $E_{\mathrm{T}}^{\mathrm{miss}}$, is a powerful discrimination quantity, due to the large expected mass of the T. The signal regions require $S_{\mathrm{T}} > 1900\,\mathrm{GeV}$, while regions to constrain the background nuisance parameters and normalisations require $1400 < S_{\mathrm{T}} < 1900\,\mathrm{GeV}$. The control and signal regions are further divided by Δm_{VLQ}, as illustrated in Figure 2. Events in these regions are used in the final likelihood fit as described below. The signal region is defined by $S_{\mathrm{T}} > 1900\,\mathrm{GeV}$

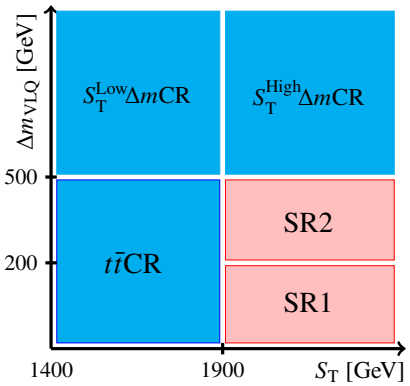

Figure 2: Illustration of the two-dimensional plane in S_T and Δm_{VLQ} on which the signal and control regions, included in the final combined likelihood fit, are defined.

and $\Delta m_{VLQ} < 500$ GeV, which is further divided into the regions SR1 with $\Delta m_{VLQ} < 200$ GeV and SR2 with $200 < \Delta m_{VLQ} < 500$ GeV. The region SR1 is designed to capture the best-reconstructed VLQ events that would have a narrow peak in the m_T^{lep} and m_T^{had} distributions. The region SR2 will capture less-well-reconstructed VLQ events, resulting in broader mass distributions. Despite this, the fraction of VLQs expected to enter this region is non-negligible. A control region with $S_T > 1900$ GeV and $\Delta m_{VLQ} > 500$ GeV, called $S_T^{High}\Delta m$CR, has low signal contamination for signal masses which are not excluded yet and is dominated by single top production. This control region provides an opportunity to constrain the modelling of the single top background using events with kinematic properties similar to the signal region. The region with $1400 < S_T < 1900$ GeV is divided into two control regions in Δm_{VLQ}: $t\bar{t}$CR with $\Delta m_{VLQ} < 500$ GeV and $S_T^{Low}\Delta m$CR with $\Delta m_{VLQ} > 500$ GeV. The $t\bar{t}$CR is rich in $t\bar{t}$ events with a purity of nearly 70% allowing constraint of the normalisation and modelling of top quark pair production. The $S_T^{Low}\Delta m$CR provides a second region for constraining the single top background, but with kinematics properties similar to the $t\bar{t}$CR. A summary of all regions is provided in Table 1. The regions not included in the fit, W+jetsCR and $t\bar{t}$RWR ($t\bar{t}$ reweighting region), serve to derive data-driven corrections to the background modelling and are discussed in the following section.

Table 1: An overview of the signal and control regions.

Selection	SR1 / SR2	$t\bar{t}$CR	$S_T^{Low}\Delta m$CR / $S_T^{High}\Delta m$CR	W+jetsCR	$t\bar{t}$RWR
Pre-selection	✓	✓	✓	✓	✓
$N_{\text{Large-}R\text{ Jet}}$	≥ 1	≥ 1	≥ 1	≥ 1	≥ 1
S_T/GeV	>1900	1400–1900	1400–1900 / >1900	900–1900	>800
$N_{W\text{-tag}}$	≥ 1	≥ 1	≥ 1	0 (≥ 1 partially inverted)	≥ 1
$N_{b\text{-tagging}}$	≥ 1	≥ 1	≥ 1	≥ 1	≥ 2
$\Delta R(W\text{-tag}, b_{had})$	> 1.0	> 1.0	> 1.0	-	< 1.0
$\Delta R(\ell, \nu)$	< 0.7	< 0.7	< 0.7	< 1.0	< 1.2
Δm_{VLQ}/GeV	< 200 / 200–500	< 500	> 500	-	-
m_T^{lep}, m_T^{had}/GeV	-	-	-	-	< 700
Included in fit	yes / yes	yes	yes / yes	no	no
Goal	Optimise Signal Sensitivity	Constrain $t\bar{t}$ normalisation	Constrain single top uncertainties	Derive W+jets normalisation factor	Derive $t\bar{t}$ S_T shape reweighting

6 Background estimation

Contributions from the dominant background processes, $t\bar{t}$ and W+jets production, are estimated using MC simulation with data-driven corrections derived in dedicated control regions dominated by the respective process. The SM backgrounds containing a prompt-lepton (single top, Z+jets, diboson, etc.) are also estimated using MC simulations. Finally, the small contribution from multijet events is estimated using a data-driven approach.

A correction for W+jets events is derived in a dedicated control region referred to as the W+jetsCR. This region is constructed to be orthogonal to the signal region in particular with an inverted jet mass requirement of the hadronic W-tagging algorithm, making use of the smoothly falling spectrum of the masses of jets produced in association with a W boson. Possible effects on the modelling of W+jets events due to the inversion of this requirement are investigated and taken into account with a dedicated uncertainty, which will be detailed later in this section. The W+jetsCR also requires $900 < S_{\mathrm{T}} < 1900$ GeV to reduce possible contamination from VLQ signal events. All other selection requirements are the same as in the signal region, as shown in Table 1.

Requiring at least one b-tagged jet as in the signal region causes the W+jetsCR to have a significant contribution from $t\bar{t}$ events. This requirement, however, helps to validate the correction to simulated W+jets events as the modelling of W+jets depends on the heavy-flavour requirement [85]. The estimation of the W+jets correction is based on the charge asymmetry of W+jets events in the W+jetsCR, present due to the asymmetry in u and d quark content in the proton [86]. At a collision centre-of-mass energy of 8 TeV, the ratio between the fiducial cross sections of W^+ and W^--boson production has been measured as $r = \sigma_{W^+}/\sigma_{W^-} = 1.4558 \pm 0.0004(\mathrm{stat.}) \pm 0.0040(\mathrm{syst.})$ [87]. Charge asymmetry is defined as $A = N_+ - N_-$, where N_+ and N_- are the numbers of events with a positively or negatively charged lepton, respectively. The correction factor to the W+jets normalisation is calculated by comparing A in data and MC simulation in the W+jetsCR. This approach decouples the charge-asymmetric process, W+jets, from possible mis-modelling of the $t\bar{t}$ events, which is a charge-symmetric process. This method is also useful for separating charge-asymmetric events from the VLQ signal, as it is also charge-symmetric.

The contributions to A from charge-symmetric backgrounds, such as $t\bar{t}$ and multijet, cancel. The small contributions from other charge-asymmetric backgrounds, such as single top, diboson, and t-associated production, is accounted for using MC samples. The dependence of the W+jets normalisation on S_{T} and the W-tag requirement was investigated in the control region sidebands (relaxed or tightened requirements on S_{T} or the W-tag selection in the W+jetsCR) to ensure applicability of this correction in the signal region. The W+jets correction is derived as a function of S_{T} up to $S_{\mathrm{T}} = 4$ TeV and no dependence of the W+jets correction on the event S_{T} is observed. An additional uncertainty is added to cover the difference in normalisation correction found in the W+jetsCR and the control region sidebands with varied W-tag requirements. The dependence of the W+jets normalisation on other relevant event and kinematic variables is checked and no significant dependencies are observed. Thus, a single normalisation factor is applied to the W+jets MC prediction. The W+jets normalisation correction amounts to $f_{W+\mathrm{jets}} = 0.915 \pm 0.09(\mathrm{stat.}) \pm 0.54(\mathrm{syst.})$, dominant systematic uncertainties are due to the uncertainty in the modelling of single top events and from the uncertainty associated with inverting the W-tag requirement.

The $t\bar{t}$ background estimate from MC simulation is known to overestimate the number of events at high t-quark p_{T} [88], directly impacting the modelling of S_{T}, which is essential for discriminating signal from background. Therefore, a data-driven reweighting is applied to the $t\bar{t}$ MC events to correct for the difference in the S_{T} distribution between the MC and data. The correction is derived in the $t\bar{t}$ reweighting region

$t\bar{t}$RWR, defined in Table 1, which has a $t\bar{t}$ purity of 89%, with the next most significant contribution from single top at 6%. The main selection criteria differentiating the $t\bar{t}$RWR from the signal region are $\Delta R(W\text{-tag}, b_{\text{had}}) < 1.0$ and $S_{\text{T}} > 800\,\text{GeV}$. These criteria are motivated by the low angular distance between the W boson and b quark from the decay of a high-p_{T} top quark. To ensure the $t\bar{t}$RWR is insensitive to signal events, the invariant masses of the reconstructed VLQs, m_T^{lep} and m_T^{had}, are required to be smaller than 700 GeV. Figure 3(a) shows the S_{T} distributions in the $t\bar{t}$RWR before deriving the reweighting.

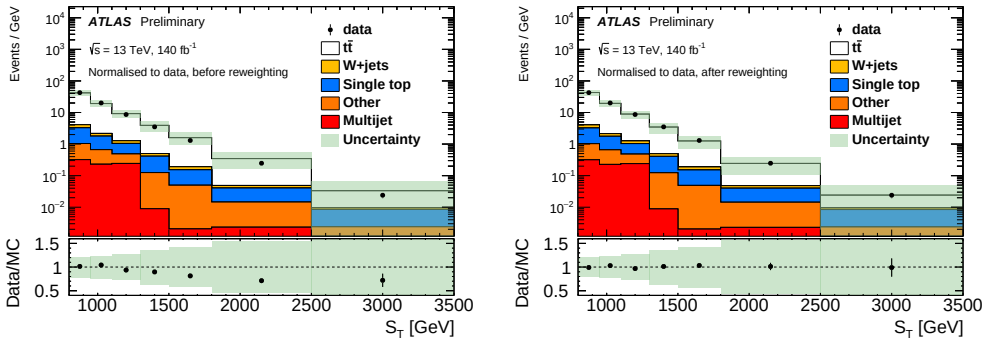

(a) (b)

Figure 3: Distributions of S_{T} for data (dots) and predictions (histograms with various colors) in the $t\bar{t}$RWR (a) before and (b) after applying the reweighting. The background is normalised to the data in order to illustrate the discrepancies in the shape of the distribution and the effect of the S_{T} shape reweighting. Uncertainties include statistical and systematic uncertainties and the last bin includes the overflow.

The reweighting is constructed to correct the shape of the S_{T} distribution, but not the normalisation, as it is freely floated in the final likelihood fit and ultimately constrained by the data in the $t\bar{t}$CR. The contributions to the $t\bar{t}$RWR from processes other than $t\bar{t}$ are subtracted from the data and the ratio of the resulting S_{T} distribution and the S_{T} distribution from the $t\bar{t}$ prediction is calculated. The correction factor is then derived in a fit to that ratio with a function of the form:

$$f(S_{\text{T}}) = p_0 \cdot \exp(-p_1 \cdot (S_{\text{T}} - p_2)^2) + p_3, \tag{1}$$

where p_i (with $i = 0, 1, 2, 3$) are the free parameters of the fit. Other functional forms are also studied, but the one in Equation (1) is found to describe the data/MC ratio most accurately. The fit is also found to be consistent for different fit intervals and bin choices. The S_{T} and the jet multiplicity N_{jets} are correlated, so the correction to S_{T} could also depend on N_{jets}. Therefore, separate fits are performed for events with $3 \leq N_{\text{jets}} \leq 6$ and $N_{\text{jets}} \geq 7$. Figure 3(b) shows the effect of the reweighting in the $t\bar{t}$RWR.

The statistical uncertainty in the fit provides an estimate of the uncertainty on the reweighted $t\bar{t}$ prediction. The impact of the uncertainty on the single top modelling is taken into account by varying the single top contribution by 100% in the $t\bar{t}$ RW region. Uncertainties on other processes have negligible impact on the extracted reweighting. The offset parameter p_3 of Equation (1) causes the function to asymptote at high values of S_{T} to 0.64 for $3 \leq N_{\text{jets}} \leq 6$ and 0.62 for $N_{\text{jets}} \geq 7$, where the statistical uncertainty is too large to determine the exact dependence of the correction on S_T with confidence. In addition, an uncertainty of 58% (38%), covering the large statistical uncertainty in the high-S_{T} tail, is added if $S_{\text{T}} \geq 2.5\,\text{TeV}$ for events with $3 \leq N_{\text{jets}} \leq 6$ ($N_{\text{jets}} \geq 7$). Finally, the correction in S_{T} was tested in a dedicated $t\bar{t}$-dominated validation region, where the $t\bar{t}$ MC estimate is found to have good agreement with data after application of the S_{T}-dependent correction.

Events from multijet production satisfy the lepton requirement of the signal region via the mis-identification of a hadronic jet as a lepton or a non-prompt lepton from a heavy-flavour jet, collectively referred to as non-prompt leptons. The contribution from multijet production is small, accounting for about 5% of the events in the signal region. Background from these processes is estimated using a data-driven "Matrix Method" (MM) [89]. This method uses the classification of the leptons in "loose" and "tight" categories to predict the number of non-prompt leptons. Tight leptons correspond to signal leptons, as described in Section 5. Loose leptons are those that fulfill the baseline criteria, as defined in Section 5, but fail the tight lepton requirements. A "loose region" enriched in non-prompt leptons is created by changing the lepton requirement from tight to loose for the signal region selection. The number of events with prompt (non-prompt) leptons in the signal region is related to the number of events with prompt (non-prompt) leptons in the loose region by the efficiencies for prompt (non-prompt) leptons that pass the baseline lepton requirements to also pass the tight requirements; referred to as the "real efficiency" ("fake efficiency"). Therefore, once the real and fake efficiencies are determined, one can solve for the number of events with non-prompt leptons (the multijet events) in the signal region, as described in Ref. [89].

The tight lepton criteria reduces the contribution of the multijet background in the signal and control regions to very low levels, such that the shapes of differential distributions estimated by the MM are dominated by statistical fluctuations. An accurate prediction for the multijet background is particularly important for the m_T^{lep} distribution, as it is used in the final likelihood fit. As the background events do not contain real VLQ decays, the distribution of reconstructed masses is largely determined by the kinematic constraints. As a result, the m_T^{lep} distribution in Z+jets and multijet events are very similar. Therefore, in the fit, the Z+jets prediction is used to model the distribution of the multijet background, scaled to the total predicted yield from the MM calculation.

For reconstructed m_T^{lep} below 200 GeV, the MM estimation of the multijet background is highly sensitive to the predicted amount of $t\bar{t}$ that is subtracted from the data. Therefore, an iterative method is employed to calculate the multijet normalisation factor. First, the multijet normalisation factor is calculated for reconstructed invariant masses above 200 GeV. Next, the $t\bar{t}$ normalisation parameter is set such that the Z+jets and the multijet predicted yields match. This is repeated until the normalisation factor changes by less than 1% from the previous iteration. A 100% uncertainty covering the modelling systematics of the prompt lepton processes and the fake lepton efficiency is applied to the multijet estimate. An additional uncorrelated 100% uncertainty (with respect to the predicted normalisation factor) on the distribution shape is applied to the multijet estimate for reconstructed invariant masses below 200 GeV to consider the special sensitivity to the $t\bar{t}$ event modelling. To model the multijet shape in other analysis regions and variables, the MC generated multijet background simulation, scaled to the MM estimate, is used.

7 Systematic uncertainties

Systematic uncertainties can be broadly grouped into the following two classes: experimental uncertainties, which are related to the modelling of the detector response and reconstruction of physics objects, and to the data-driven background estimation or the data-driven corrections to the simulated backgrounds; theoretical uncertainties, which are related to the modelling of the physics processes by simulation. Unless stated otherwise, uncertainties from a common source are correlated across processes and regions in the final statistical analysis and the impact of the uncertainties is allowed to be constrained by the likelihood fit to the data.

The dominant systematic uncertainties in this search are those related to the modelling of the $t\bar{t}$ and single top backgrounds. The theory uncertainties for the $t\bar{t}$ prediction include the impact of the choice of MC generator (in this case, MC events were generated to NLO precision); ISR, FSR, and parton shower model; and shower matching scheme of simulated $t\bar{t}$ events, each of which is evaluated by comparing the nominal $t\bar{t}$ prediction to the alternative MC samples, as described in Section 3. Modelling uncertainties on the single top prediction include the choice of the parton shower and the matching of the NLO matrix element to the parton shower, which are evaluated using alternate samples as described in Section 3. Similarly, an uncertainty due to the choice of the $t\bar{t}/Wt$ overlap removal scheme is evaluated by comparing the nominal single top MC produced with DR scheme to the alternative sample produced with the DS scheme [42, 48, 90]. The data are found to be more compatible with the DR scheme at lower energies, while at higher energies, the DS scheme is observed to be more compatible. To avoid extrapolation of the DS versus DR uncertainty from the regions defined with low S_{T} to those at high S_{T}, this uncertainty is split into a high-S_{T} component, applied to regions with $S_{\mathrm{T}} > 1.9\,\mathrm{TeV}$, and a low-$S_{\mathrm{T}}$ component, applied to regions with $1.4 < S_{\mathrm{T}} < 1.9\,\mathrm{TeV}$. For both single top and $t\bar{t}$ production, uncertainties associated with the choice of the PDF are obtained using the `PDF4LHC15` combined PDF set [91] . The effect of QCD scale uncertainties is estimated by independently doubling or halving the renormalisation and factorisation scales in case of single top and $t\bar{t}$ production. The QCD scale variation with the largest impact on the fit discriminant (m_T^{lep}) is used.

To simplify the statistical analysis, all subdominant backgrounds from $t\bar{t}V$, Z+jets, rare top processes and diboson production are grouped into a single category named "other", and a single overall normalisation uncertainty of 50% is applied. This uncertainty of 50% is adopted from the uncertainty on Z+jets events which has the largest relative uncertainty among the processes contained in the "other" category. The uncertainty on the Z+jets contribution was estimated in the previous analysis [18] by investigating the mismodeling of the jet multiplicity of Z+jets events.

Experimental uncertainties include the uncertainity of 0.83% on the integrated luminosity measurement on the combined 2015−2018 data [22], obtained using the LUCID-2 detector [23] for the primary luminosity measurements. Uncertainties on leptons arise from potential mismodelling of the electron and muon energy scales and resolutions [64, 65] as well as from uncertainties on the correction factors to the electron and muon trigger, reconstruction, identification and isolation efficiencies [64, 66].

Uncertainties on the small-R jets include uncertainties on the JES, the JER [69] and on the JMS [80]. An uncertainy is assigned to the JVT selection efficiency [92] and to the reweighting factors that correct the pile-up profile in MC simulations to match that in data. Similarly, JES, JER [80] and JMS uncertainties, and in addition JMR [81] systematics are assigned to large-radius jets. An uncertainty related to the scale and resolution of the track soft term in the $E_{\mathrm{T}}^{\mathrm{miss}}$ calculation [93] is applied.

Uncertainties on the b-tagging algorithm selection efficiency include uncertainties on the b-jet selection efficiency, c-jet and light jet mistag rate correction factors and additional components from the extrapolation of the calibrations to high p_{T} and from c-jets to τ leptons [73, 75, 76]. An uncertainty is assigned to the efficiency correction of the W-tagging algorithm [82, 84].

Uncertainties on the data-driven corrections for simulated backgrounds or on the data-driven multijet event estimate are briefly listed below and detailed in Section 6. The uncertainty on the data-driven correction on simulated W+jets events is 60%. The uncertainty on the $t\bar{t}$ S_{T} shape reweighting consists of a statistical component and a systematic component from the uncertainty on the single top contribution in the $t\bar{t}$RWR. The two components affecting the multijet background estimation include a global 100% uncertainty on

the MM estimate and an additional 100% uncertainty for reconstructed VLQ invariant masses m_T^{lep} below 200 GeV.

8 Statistical analysis and results

To test for the presence of the VLQ signal, a fit is performed using the reconstructed mass distributions of the leptonically decaying T candidate (m_T^{lep}) from the signal regions SR1 and SR2 and control regions $t\bar{t}$CR, $S_{\text{T}}^{\text{Low}}\Delta m$CR, and $S_{\text{T}}^{\text{High}}\Delta m$CR. The mass of the leptonically decaying T is chosen as its resolution was shown to be better than that of the hadronically decaying T. The fit maximises a binned likelihood function $\mathcal{L}(\mu, \boldsymbol{\theta})$ constructed as a product of Poisson probabilities for all bins considered in the search and depends on the parameter of interested μ and vector of nuisance parameters (NP) $\boldsymbol{\theta}$. The parameter of interest is the signal strength $\mu = \sigma^{\text{test}}/\sigma^{\text{theory}}$, where σ^{test} is the value for the VLQ cross section being tested and σ^{theory} is the theoretical prediction. Each NP θ_i encodes a systematic uncertainty with a Gaussian prior, except the normalisations of the $t\bar{t}$ and single top backgrounds, which are unconstrained, and the statistical uncertainties due to the finite size of the MC samples, which are included as bin-by-bin NPs with Poisson uncertainties. If an uncertainty would impact the normalisation or shape of all bins for a given process by less than 1%, the NP is removed from the fit for that process. The test statistic q_μ is defined as the profile likelihood ratio, $q_\mu = -2\ln(\mathcal{L}(\mu, \hat{\hat{\boldsymbol{\theta}}}_\mu)/\mathcal{L}(\hat{\mu}, \hat{\boldsymbol{\theta}}))$, where $\hat{\mu}$ and $\hat{\boldsymbol{\theta}}$ are the values of the parameters that maximise the likelihood function (with the constraint $0 \leq \hat{\mu} \leq \mu$), and $\hat{\hat{\boldsymbol{\theta}}}_\mu$ are the values of the nuisance parameters that maximise the likelihood function for a given value of μ. The compatibility of the observed data with the background-only hypothesis is tested by setting $\mu = 0$ in the profile likelihood ratio. Upper limits on the cross section times branching ratio for a given signal are derived by using q_μ in the CL_s method [94, 95], approximated using the asymptotic formulae [96]. For a given signal, the cross section times branching ratio is excluded at $\geq 95\%$ confidence level (CL) when $\text{CL}_\text{s} < 0.05$ [96].

Figure 4 shows the m_T^{lep} distribution in each of the five fit regions after the simultaneous fit of the background-only hypothesis to data. The corresponding event yields are listed in Table 2. The uncertainty on the total prediction does not equal the sum in quadrature of the individual component due to correlations between the fit parameters. The expected numbers of $T\bar{T}$ signal events in the five fit regions are given in Table 3 for various VLQ scenarios. The compatibility of the data with the background-only hypothesis is estimated by integrating the distribution of the test statistic above the observed value of q_0. This value is computed for each signal scenario considered, defined by the assumed mass of the heavy quark and the three decay branching ratios. These results assume the T has a narrow width.

No significant excess above the background expectation is found. Upper limits at the 95% CL on the $T\bar{T}$ production cross section are set for two benchmark scenarios as a function of T quark mass m_{VLQ} and compared to the theoretical prediction from Top++ 2.0 (see Figure 5). The resulting lower limit on m_{VLQ} is determined using the central value of the theoretical cross section prediction.

For T masses from 1000 GeV to 2000 GeV and $\mathcal{B}(T \to Wb) = 1$, the data exclude $T\bar{T}$ production cross sections above 10.1 fb to 0.27 fb at 95% CL. Comparing to the theory cross section, this results in an observed (expected) lower limit on the T mass of $m_{\text{VLQ}} > 1700$ GeV (1570 GeV) for this scenario. For branching ratios corresponding to the SU(2) singlet T scenario, the observed (expected) 95% CL lower mass limit is $m_{\text{VLQ}} > 1420$ GeV (1410 GeV). The sensitivity of the analysis is limited by the statistical uncertainty of the data. Including all systematic uncertainties for the $\mathcal{B}(T \to Wb) = 1$ scenario degrades

Table 2: Event yields in the five fit regions after the fit of SM processes to the data. The uncertainties include statistical and systematic uncertainties. The uncertainties in the individual background components can be larger than the uncertainty in the sum of the backgrounds due to correlations.

	SR1	SR2	$S_{\mathrm{T}}^{\mathrm{High}}\Delta m$CR	$t\bar{t}$CR	$S_{\mathrm{T}}^{\mathrm{Low}}\Delta m$CR
$t\bar{t}$	257 ± 33	74 ± 14	46 ± 9	1513 ± 150	127 ± 18
W+jets	61 ± 25	17 ± 7	12 ± 5	213 ± 90	24 ± 10
Single top	53 ± 19	40 ± 14	23 ± 10	340 ± 120	60 ± 20
Other	48 ± 21	15 ± 7	7.5 ± 3.4	160 ± 70	14 ± 6
Multijet	3 ± 11	0.9 ± 3.1	0.7 ± 2.4	10 ± 40	1 ± 5
Total	422 ± 21	146 ± 11	89 ± 8	2240 ± 60	226 ± 13
Data	430	142	83	2235	232

Table 3: Expected $T\bar{T}$ event yields in the five fit regions for various VLQ scenarios. The uncertainties include statistical and systematic uncertainties.

	SR1	SR2	$S_{\mathrm{T}}^{\mathrm{High}}\Delta m$CR	$t\bar{t}$CR	$S_{\mathrm{T}}^{\mathrm{Low}}\Delta m$CR
$\mathcal{B}(T \to Wb) = 1$:					
$m_{\mathrm{VLQ}} = 1200\,\mathrm{GeV}$	83 ± 4	26.9 ± 1.3	9.5 ± 0.6	18.7 ± 0.6	1.34 ± 0.08
$m_{\mathrm{VLQ}} = 1400\,\mathrm{GeV}$	27.6 ± 1.7	10.6 ± 0.7	4.6 ± 0.4	2.41 ± 0.10	0.248 ± 0.022
$m_{\mathrm{VLQ}} = 1400\,\mathrm{GeV}$	8.6 ± 0.6	3.59 ± 0.24	1.87 ± 0.14	0.273 ± 0.017	0.051 ± 0.004
$m_{\mathrm{VLQ}} = 1400\,\mathrm{GeV}$	2.69 ± 0.23	1.47 ± 0.11	0.81 ± 0.06	0.057 ± 0.006	0.010 ± 0.001
Singlet T :					
$m_{\mathrm{VLQ}} = 1200\,\mathrm{GeV}$	56.9 ± 3.0	29.0 ± 1.7	14.6 ± 1.2	17.2 ± 0.7	1.34 ± 0.08
$m_{\mathrm{VLQ}} = 1400\,\mathrm{GeV}$	19.8 ± 1.2	10.7 ± 0.7	6.2 ± 0.5	2.36 ± 0.11	0.248 ± 0.022
$m_{\mathrm{VLQ}} = 1400\,\mathrm{GeV}$	6.2 ± 0.4	3.62 ± 0.25	2.65 ± 0.22	0.346 ± 0.017	0.051 ± 0.004
$m_{\mathrm{VLQ}} = 1400\,\mathrm{GeV}$	2.08 ± 0.17	1.29 ± 0.10	1.07 ± 0.09	0.074 ± 0.003	0.010 ± 0.001

the expected cross section limit by less than 3.7% for any of the tested masses, and reduces the expected mass limit by only 10 GeV.

In general, the prediction is found to overestimate the data, especially in the high mass tails of the m_T^{lep} distribution. Therefore, the observed limits on the signal cross section, and thus also on the signal mass m_{VLQ}, are more generally stringent than the expected limits. Large bin-to-bin variations between 1000 to 1600 GeV in the m_T^{lep} distribution are observed in SR1, with an excess relative to the prediction in one bin and deficits in three bins. However, no signal model is compatible with the narrow excess in SR1, as the width of the m_T^{lep} distributions are all much wider than the observed one-bin excess. Additionally, no such excess or large bin-to-bin variations of the data are observed in SR2. This narrow excess in SR1 does, however, lead to weaker observed cross section limits in an m_{VLQ} interval between around 1250 GeV to 1500 GeV with respect to the rest of the m_{VLQ} spectrum.

In the previous search by ATLAS performed on a part of this data set with an integrated luminosity of 36 fb^{-1} [18], observed (expected) 95% CL mass limits of 1350 GeV (1310 GeV) for the scenario $\mathcal{B}(T \to Wb) = 1$ and 1170 GeV (1080 GeV) for a singlet T were found. The present search thus extends the observed mass limits by 350 GeV and 250 GeV for the $\mathcal{B}(T \to Wb) = 1$ and singlet T case, respectively. The increase of the mass limits can almost entirely be attributed to the increase of the data set from 36 fb^{-1} to 140 fb^{-1}, but about 15% (20%) of the improvements on the scenario $\mathcal{B}(T \to Wb) = 1$ (singlet T scenario) mass limit is expected to come from changes in the analysis strategy, especially from improvements to the

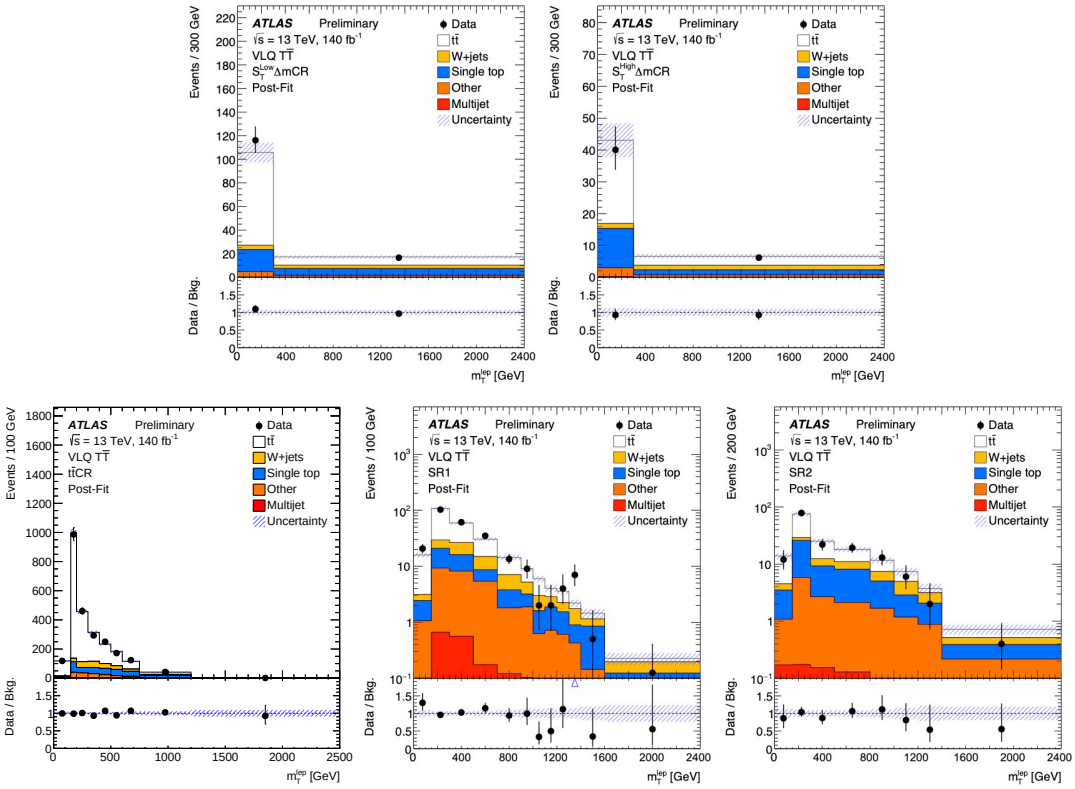

Figure 4: The distribution for m_T^{lep} in the five fit regions ($S_{\text{T}}^{\text{Low}}\Delta m$CR, $S_{\text{T}}^{\text{High}}\Delta m$CR, $t\bar{t}$CR, SR1, and SR2, respectively) after the simultaneous fit of the background-only hypothesis to data. The lower panels of each plot shows the ratio of data to the fitted background yields with overflow included in the last bin. The band represents the systematic uncertainty after the maximum-likelihood fit.

W-boson tagging and the slicing of the signal region into two regions, SR1 and SR2 according to the event Δm_{VLQ}.

To check that the results do not depend on the weak-isospin of the T quark in the simulated signal events, a sample of $T\bar{T}$ events with a mass of 1.2 TeV was generated for an SU(2) doublet T quark and compared to the nominal sample of the same mass generated with an SU(2) singlet T quark. Both the expected number of events and expected excluded cross section are consistent between those two samples. Thus the limits obtained are also applicable to VLQ models with non-zero weak-isospin. As there is no explicit use of charge identification, the $\mathcal{B}(T \to Wb) = 1$ limits are applicable to the pair-production of vector-like Y quarks of charge $-4/3$, which decay exclusively to Wb.

In addition to the benchmark scenarios, other combinations of T branching ratios can be tested by reweighting the relative contributions of the three T decay modes. Figure 6 shows the expected and observed lower limits on the T mass as a function of $\mathcal{B}(T \to Wb)$ and $\mathcal{B}(T \to Ht)$. For each point in the figure, the branching ratios for $T \to Zt$ decay are determined by the requirement $\mathcal{B}(T \to Wb) + \mathcal{B}(T \to Ht) + \mathcal{B}(T \to Zt) = 1$. Although the analysis is designed to search for $T\bar{T}$, it also has sensitivity to $B\bar{B}$ production. Figure 7 shows the expected and observed lower limits on the B mass as a function of $\mathcal{B}(B \to Wt)$ and $\mathcal{B}(B \to Hb)$, with $\mathcal{B}(B \to Zb) = 1 - \mathcal{B}(B \to Wt) - \mathcal{B}(B \to Hb)$.

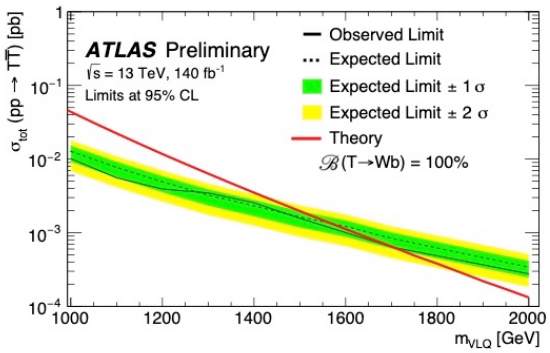

(a)

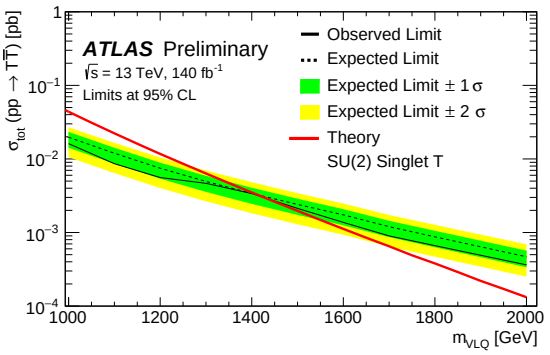

(b)

Figure 5: Expected (dashed black line) and observed (solid black line) upper limits at the 95% CL on the $T\bar{T}$ cross section as a function of T quark mass for (a) the $\mathcal{B}(T \to Wb) = 1$ scenario and (b) in the SU(2) singlet T . The green and yellow bands correspond to ±1 and ±2 standard deviations around the expected limit. The thin red line and band show the theoretical prediction and its ±1 standard deviation uncertainty.

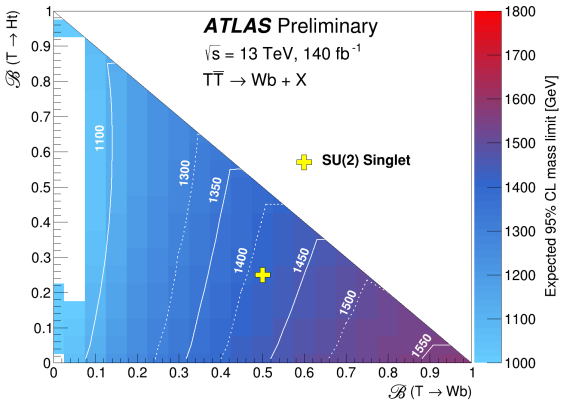

(a)

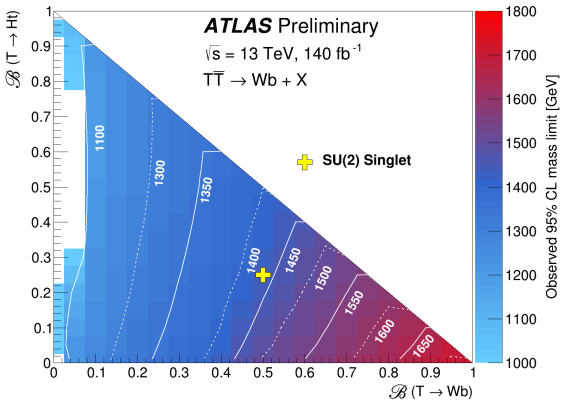

(b)

Figure 6: (a) Expected and (b) observed 95% CL lower limits on the mass of the T quark in the branching-ratio plane of $\mathcal{B}(T \to Wb)$ versus $\mathcal{B}(T \to Ht)$. Contour lines are provided to guide the eye. The white region is due to the limit falling below 1000GeV, the lowest signal mass considered in this search.

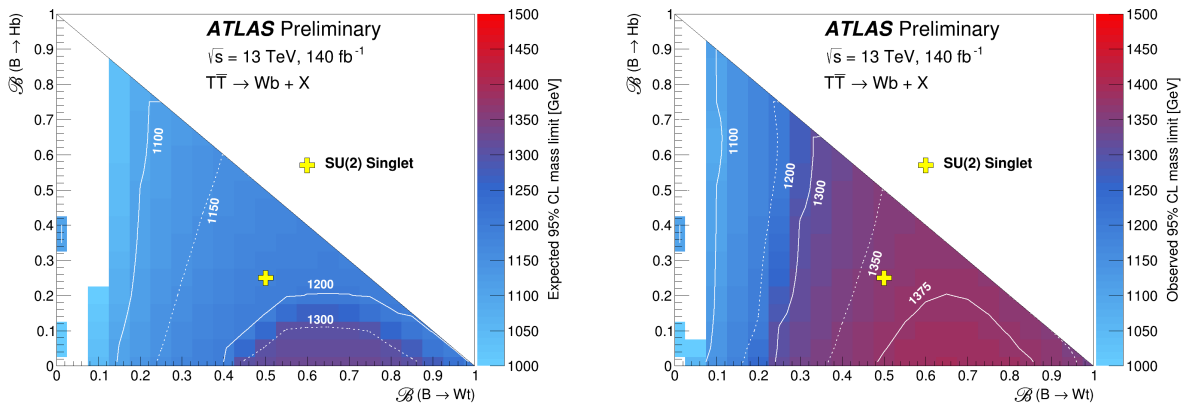

(a) (b)

Figure 7: (a) Expected and (b) observed 95% CL lower limits on the mass of the B quark in the branching-ratio plane of $\mathcal{B}(B \to Wt)$ versus $\mathcal{B}(B \to Hb)$. Contour lines are provided to guide the eye. The white region is due to the limit falling below 1000GeV, the lowest signal mass considered in this search.

9 Conclusion

A search for pair-produced vector-like T quarks was performed in events with exactly one electron or muon, missing transverse momentum and jets using the full Run 2 ATLAS data set. Final states compatible with the decay of a pair of heavy vector-like quarks were selected and a combined fit was performed using the mass of the reconstructed vector-like quark in three control regions and two signal regions. No significant excess over the background expectation is observed and 95% CL upper limits were set on the vector-like quark cross section and lower bounds were set on the vector-like quark mass. The search is optimised for $T\bar{T} \to WbWb$, thus the most stringent limits are set for the scenario $\mathcal{B}(T \to Wb) = 1$, for which masses below 1700 GeV (1570 GeV) are observed (expected) to be excluded at 95% CL. The limits for $\mathcal{B}(T \to Wb) = 1$ also apply to a vector-like Y quark with charge $-4/3$, which decays exclusively to Wb. The observed (expected) lower mass limit for the weak isospin singlet T model is 1420 GeV (1410 GeV) and limits for other T branching ratios are presented in the plane of $\mathcal{B}(T \to Wb)$ vs. $\mathcal{B}(T \to Ht)$. The analysis was also used to set limits on the mass of B quarks as a function of branching ratios. This search improves the previous result that used 36 fb^{-1} of ATLAS data by 350 GeV for the scenario $\mathcal{B}(T \to Wb) = 1$ and by 250 GeV in the T singlet case.

References

[1] L. Susskind, *Dynamics of spontaneous symmetry breaking in the Weinberg-Salam theory*, Phys. Rev. D **20** (1979) 2619 (cit. on p. 2).

[2] L. Randall and R. Sundrum, *Large Mass Hierarchy from a Small Extra Dimension*, Phys. Rev. Lett. **83** (1999) 3370, arXiv: hep-ph/9905221 (cit. on p. 2).

[3] D. B. Kaplan, H. Georgi, H. and S. Dimopoulos, *Composite Higgs scalars*, Phys. Lett. B **136** (1984) 187 (cit. on p. 2).

[4] N. Vignaroli, *Discovering the composite Higgs through the decay of a heavy fermion*, JHEP **07** (2012) 158, arXiv: 1204.0468 [hep-ph] (cit. on p. 2).

[5] M. Schmaltz and D. Tucker-Smith, *Little Higgs Theories*, Ann. Rev. Nucl. Part. Sci. **55** (2005) 229, arXiv: hep-ph/0502182 (cit. on p. 2).

[6] J. A. Aguilar-Saavedra, R. Benbrik, S. Heinemeyer and M. Pérez-Victoria, *Handbook of vectorlike quarks: Mixing and single production*, Phys. Rev. D **88** (2013) 094010, arXiv: 1306.0572 [hep-ph] (cit. on p. 2).

[7] O. Eberhardt et al., *Impact of a Higgs Boson at a Mass of 126 GeV on the Standard Model with Three and Four Fermion Generations*, Phys. Rev. Lett. **109** (2012) 241802, arXiv: 1209.1101 [hep-ph] (cit. on p. 2).

[8] ATLAS Collaboration, *Combination of the Searches for Pair-Produced Vectorlike Partners of the Third-Generation Quarks at $\sqrt{s} = 13$ TeV with the ATLAS Detector*, Phys. Rev. Lett. **121** (2018) 211801, arXiv: 1808.02343 [hep-ex] (cit. on p. 2).

[9] ATLAS Collaboration, *Search for pair-produced vector-like top and bottom partners in events with large missing transverse momentum in pp collisions with the ATLAS detector*, Eur. Phys. J. C **83** (2023) 719, arXiv: 2212.05263 [hep-ex] (cit. on p. 2).

[10] ATLAS Collaboration, *Search for pair-production of vector-like quarks in pp collision events at $\sqrt{s} = 13$ TeV with at least one leptonically decaying Z boson and a third-generation quark with the ATLAS detector*, Phys. Lett. B **843** (2023) 138019, arXiv: 2210.15413 [hep-ex] (cit. on p. 2).

[11] ATLAS Collaboration, *Search for single production of vector-like T quarks decaying into Ht or Zt in pp collisions at $\sqrt{s} = 13$ TeV with the ATLAS detector*, JHEP **08** (2023) 153, arXiv: 2305.03401 [hep-ex] (cit. on p. 2).

[12] ATLAS Collaboration, *Search for single production of a vectorlike T quark decaying into a Higgs boson and top quark with fully hadronic final states using the ATLAS detector*, Phys. Rev. D **105** (2022) 092012, arXiv: 2201.07045 [hep-ex] (cit. on p. 2).

[13] A. Roy, N. Nikiforou, N. Castro and T. Andeen, *Novel interpretation strategy for searches of singly produced vectorlike quarks at the LHC*, Phys. Rev. D **101** (2020) 115027, arXiv: 2003.00640 [hep-ex] (cit. on p. 2).

[14] CMS Collaboration, *A search for bottom-type, vector-like quark pair production in a fully hadronic final state in proton–proton collisions at $\sqrt{s} = 13$ TeV*, Phys. Rev. D **102** (2020) 112004, arXiv: 2008.09835 [hep-ex] (cit. on p. 3).

[15] CMS Collaboration, *Search for single production of a vector-like T quark decaying to a top quark and a Z boson in the final state with jets and missing transverse momentum at $\sqrt{s} = 13$ TeV*, JHEP **05** (2022) 93, arXiv: 2201.02227 [hep-ex] (cit. on p. 3).

[16] CMS Collaboration, *Search for a heavy resonance decaying into a top quark and a W boson in the lepton+jets final state at* $\sqrt{s} = 13$ *TeV*, JHEP **04** (2021) 048, arXiv: 2111.10216 [hep-ex] (cit. on p. 3).

[17] CMS Collaboration, *Search for a vector-like quark* $T' \to tH$ *via the diphoton decay mode of the Higgs boson in proton-proton collisions at* $\sqrt{s} = 13$ *TeV*, JHEP **09** (2023) 057, arXiv: 2302.12802 [hep-ex] (cit. on p. 3).

[18] ATLAS Collaboration, *Search for pair production of heavy vector-like quarks decaying to high-*p_T *W bosons and b quarks in the lepton-plus-jets final state in* pp *collisions at* $\sqrt{s} = 13$ *TeV with the ATLAS detector*, JHEP **10** (2017) 141, arXiv: 1707.03347 [hep-ex] (cit. on pp. 3, 8, 13, 15).

[19] CMS Collaboration, *Search for pair production of vector-like quarks in leptonic final states in proton-proton collisions at* $\sqrt{s} = 13$ *TeV*, JHEP **07** (2023) 020, arXiv: 2209.07327 [hep-ex] (cit. on p. 3).

[20] ATLAS Collaboration, *The ATLAS Experiment at the CERN Large Hadron Collider*, JINST **3** (2008) S08003 (cit. on p. 3).

[21] ATLAS Collaboration, *The ATLAS Collaboration Software and Firmware*, ATL-SOFT-PUB-2021-001, 2021, URL: https://cds.cern.ch/record/2767187 (cit. on p. 3).

[22] ATLAS Collaboration, *Luminosity determination in* pp *collisions at* $\sqrt{s} = 13$ *TeV using the ATLAS detector at the LHC*, arXiv: 2212.09379 [hep-ex] (cit. on pp. 4, 13).

[23] G. Avoni et al., *The new LUCID-2 detector for luminosity measurement and monitoring in ATLAS*, JINST **13** (2018) P07017 (cit. on pp. 4, 13).

[24] ATLAS Collaboration, *Performance of electron and photon triggers in ATLAS during LHC Run 2*, Eur. Phys. J. C **80** (2020) 47, arXiv: 1909.00761 [hep-ex] (cit. on p. 4).

[25] ATLAS Collaboration, *Performance of the ATLAS muon triggers in Run 2*, JINST **15** (2020) P09015, arXiv: 2004.13447 [physics.ins-det] (cit. on p. 4).

[26] ATLAS Collaboration, *ATLAS data quality operations and performance for 2015–2018 data-taking*, JINST **15** (2020) P04003, arXiv: 1911.04632 [physics.ins-det] (cit. on p. 4).

[27] ATLAS Collaboration, *The ATLAS Simulation Infrastructure*, Eur. Phys. J. C **70** (2010) 823, arXiv: 1005.4568 [physics.ins-det] (cit. on p. 4).

[28] GEANT4 Collaboration, S. Agostinelli et al., *GEANT4 – a simulation toolkit*, Nucl. Instrum. Meth. A **506** (2003) 250 (cit. on p. 4).

[29] ATLAS Collaboration, *The simulation principle and performance of the ATLAS fast calorimeter simulation FastCaloSim*, ATL-PHYS-PUB-2010-013, 2010, URL: https://cds.cern.ch/record/1300517 (cit. on p. 4).

[30] T. Sjöstrand et al., *An introduction to PYTHIA 8.2*, Comput. Phys. Commun. **191** (2015) 159, arXiv: 1410.3012 [hep-ph] (cit. on p. 4).

[31] ATLAS Collaboration, *ATLAS Pythia 8 tunes to 7 TeV data*, ATL-PHYS-PUB-2014-021, 2014, URL: https://cds.cern.ch/record/1966419 (cit. on p. 4).

[32] NNPDF Collaboration, R. D. Ball et al., *Parton distributions with LHC data*, Nucl. Phys. B **867** (2013) 244, arXiv: 1207.1303 [hep-ph] (cit. on p. 4).

[33] T. Sjöstrand, S. Mrenna and P. Skands, *A brief introduction to PYTHIA 8.1*, Comput. Phys. Commun. **178** (2008) 852, arXiv: 0710.3820 [hep-ph] (cit. on p. 4).

[34] ATLAS Collaboration, *The Pythia 8 A3 tune description of ATLAS minimum bias and inelastic measurements incorporating the Donnachie–Landshoff diffractive model*, ATL-PHYS-PUB-2016-017, 2016, URL: https://cds.cern.ch/record/2206965 (cit. on p. 4).

[35] J. A. Aguilar-Saavedra, *Identifying top partners at LHC*, JHEP **11** (2009) 030, arXiv: 0907.3155 [hep-ph] (cit. on p. 4).

[36] M. Czakon and A. Mitov, *Top++: A program for the calculation of the top-pair cross-section at hadron colliders*, Comput. Phys. Commun. **185** (2014) 2930, arXiv: 1112.5675 [hep-ph] (cit. on p. 4).

[37] S. Frixione, G. Ridolfi and P. Nason, *A positive-weight next-to-leading-order Monte Carlo for heavy flavour hadroproduction*, JHEP **09** (2007) 126, arXiv: 0707.3088 [hep-ph] (cit. on p. 4).

[38] P. Nason, *A new method for combining NLO QCD with shower Monte Carlo algorithms*, JHEP **11** (2004) 040, arXiv: hep-ph/0409146 (cit. on pp. 4, 5).

[39] S. Frixione, P. Nason and C. Oleari, *Matching NLO QCD computations with parton shower simulations: the POWHEG method*, JHEP **11** (2007) 070, arXiv: 0709.2092 [hep-ph] (cit. on pp. 4, 5).

[40] S. Alioli, P. Nason, C. Oleari and E. Re, *A general framework for implementing NLO calculations in shower Monte Carlo programs: the POWHEG BOX*, JHEP **06** (2010) 043, arXiv: 1002.2581 [hep-ph] (cit. on pp. 4, 5).

[41] NNPDF Collaboration, R. D. Ball et al., *Parton distributions for the LHC run II*, JHEP **04** (2015) 040, arXiv: 1410.8849 [hep-ph] (cit. on pp. 4, 5).

[42] ATLAS Collaboration, *Studies on top-quark Monte Carlo modelling for Top2016*, ATL-PHYS-PUB-2016-020, 2016, URL: https://cds.cern.ch/record/2216168 (cit. on pp. 4, 5, 13).

[43] M. Bähr et al., *Herwig++ physics and manual*, Eur. Phys. J. C **58** (2008) 639, arXiv: 0803.0883 [hep-ph] (cit. on p. 5).

[44] J. Bellm et al., *Herwig 7.0/Herwig++ 3.0 release note*, Eur. Phys. J. C **76** (2016) 196, arXiv: 1512.01178 [hep-ph] (cit. on p. 5).

[45] L. A. Harland-Lang, A. D. Martin, P. Motylinski and R. S. Thorne, *Parton distributions in the LHC era: MMHT 2014 PDFs*, Eur. Phys. J. C **75** (2015) 204, arXiv: 1412.3989 [hep-ph] (cit. on p. 5).

[46] J. Alwall et al., *The automated computation of tree-level and next-to-leading order differential cross sections, and their matching to parton shower simulations*, JHEP **07** (2014) 079, arXiv: 1405.0301 [hep-ph] (cit. on p. 5).

[47] ATLAS Collaboration, *Study of top-quark pair modelling and uncertainties using ATLAS measurements at* $\sqrt{s} = 13$ *TeV*, ATL-PHYS-PUB-2020-023, 2020, URL: https://cds.cern.ch/record/2730443 (cit. on p. 5).

[48] S. Frixione, E. Laenen, P. Motylinski, C. White and B. R. Webber, *Single-top hadroproduction in association with a W boson*, JHEP **07** (2008) 029, arXiv: 0805.3067 [hep-ph] (cit. on pp. 5, 6, 13).

[49] R. Frederix, E. Re and P. Torrielli,
Single-top t-channel hadroproduction in the four-flavour scheme with POWHEG and aMC@NLO,
JHEP **09** (2012) 130, arXiv: 1207.5391 [hep-ph] (cit. on p. 5).

[50] S. Alioli, P. Nason, C. Oleari and E. Re,
NLO single-top production matched with shower in POWHEG: s- and t-channel contributions,
JHEP **09** (2009) 111, arXiv: 0907.4076 [hep-ph] (cit. on p. 5), Erratum: JHEP **02** (2010) 011.

[51] E. Bothmann et al., *Event generation with Sherpa 2.2*, SciPost Phys. **7** (2019) 034,
arXiv: 1905.09127 [hep-ph] (cit. on p. 5).

[52] T. Gleisberg and S. Höche, *Comix, a new matrix element generator*, JHEP **12** (2008) 039,
arXiv: 0808.3674 [hep-ph] (cit. on p. 5).

[53] F. Buccioni et al., *OpenLoops 2*, Eur. Phys. J. C **79** (2019) 866, arXiv: 1907.13071 [hep-ph]
(cit. on p. 5).

[54] F. Cascioli, P. Maierhöfer and S. Pozzorini, *Scattering Amplitudes with Open Loops*,
Phys. Rev. Lett. **108** (2012) 111601, arXiv: 1111.5206 [hep-ph] (cit. on p. 5).

[55] A. Denner, S. Dittmaier and L. Hofer,
COLLIER: A fortran-based complex one-loop library in extended regularizations,
Comput. Phys. Commun. **212** (2017) 220, arXiv: 1604.06792 [hep-ph] (cit. on p. 5).

[56] S. Schumann and F. Krauss,
A parton shower algorithm based on Catani–Seymour dipole factorisation, JHEP **03** (2008) 038,
arXiv: 0709.1027 [hep-ph] (cit. on p. 5).

[57] S. Höche, F. Krauss, M. Schönherr and F. Siegert,
A critical appraisal of NLO+PS matching methods, JHEP **09** (2012) 049,
arXiv: 1111.1220 [hep-ph] (cit. on p. 5).

[58] S. Höche, F. Krauss, M. Schönherr and F. Siegert,
QCD matrix elements + parton showers. The NLO case, JHEP **04** (2013) 027,
arXiv: 1207.5030 [hep-ph] (cit. on p. 5).

[59] S. Catani, F. Krauss, B. R. Webber and R. Kuhn, *QCD Matrix Elements + Parton Showers*,
JHEP **11** (2001) 063, arXiv: hep-ph/0109231 (cit. on p. 5).

[60] S. Höche, F. Krauss, S. Schumann and F. Siegert, *QCD matrix elements and truncated showers*,
JHEP **05** (2009) 053, arXiv: 0903.1219 [hep-ph] (cit. on p. 5).

[61] C. Anastasiou, L. Dixon, K. Melnikov and F. Petriello, *High-precision QCD at hadron colliders:
Electroweak gauge boson rapidity distributions at next-to-next-to leading order*,
Phys. Rev. D **69** (2004) 094008, arXiv: hep-ph/0312266 (cit. on p. 5).

[62] J. Gao et al., *CT10 next-to-next-to-leading order global analysis of QCD*,
Phys. Rev. D **89** (2014) 033009, arXiv: 1302.6246 [hep-ph] (cit. on p. 6).

[63] D. J. Lange, *The EvtGen particle decay simulation package*, Nucl. Instrum. Meth. A **462** (2001) 152
(cit. on p. 6).

[64] ATLAS Collaboration, *Electron and photon performance measurements with the ATLAS detector
using the 2015–2017 LHC proton–proton collision data*, JINST **14** (2019) P12006,
arXiv: 1908.00005 [hep-ex] (cit. on pp. 6, 13).

[65] ATLAS Collaboration, *Muon reconstruction performance of the ATLAS detector in proton–proton collision data at* $\sqrt{s}$ = 13 *TeV*, Eur. Phys. J. C **76** (2016) 292, arXiv: 1603.05598 [hep-ex] (cit. on pp. 6, 13).

[66] ATLAS Collaboration, *Muon reconstruction and identification efficiency in ATLAS using the full Run 2 pp collision data set at* $\sqrt{s}$ = 13 *TeV*, Eur. Phys. J. C **81** (2021) 578, arXiv: 2012.00578 [hep-ex] (cit. on pp. 6, 13).

[67] ATLAS Collaboration, *Studies of the muon momentum calibration and performance of the ATLAS detector with pp collisions at* $\sqrt{s}$*=13 TeV*, Eur. Phys. J. C **83** (2023) 686, arXiv: 2212.07338 (cit. on p. 6).

[68] ATLAS Collaboration, *Jet reconstruction and performance using particle flow with the ATLAS Detector*, Eur. Phys. J. C **77** (2017) 466, arXiv: 1703.10485 [hep-ex] (cit. on p. 6).

[69] ATLAS Collaboration, *Jet energy scale and resolution measured in proton–proton collisions at* $\sqrt{s}$ = 13 *TeV with the ATLAS detector*, Eur. Phys. J. C **81** (2021) 689, arXiv: 2007.02645 [hep-ex] (cit. on pp. 6, 7, 13).

[70] M. Cacciari, G. P. Salam and G. Soyez, *The anti-*k_t *jet clustering algorithm*, JHEP **04** (2008) 063, arXiv: 0802.1189 [hep-ph] (cit. on p. 6).

[71] M. Cacciari, G. P. Salam and G. Soyez, *FastJet user manual*, Eur. Phys. J. C **72** (2012) 1896, arXiv: 1111.6097 [hep-ph] (cit. on p. 6).

[72] ATLAS Collaboration, *Tagging and suppression of pileup jets with the ATLAS detector*, ATLAS-CONF-2014-018, 2014, URL: https://cds.cern.ch/record/1700870 (cit. on p. 7).

[73] ATLAS Collaboration, *ATLAS b-jet identification performance and efficiency measurement with* $t\bar{t}$ *events in pp collisions at* $\sqrt{s}$ = 13 *TeV*, Eur. Phys. J. C **79** (2019) 970, arXiv: 1907.05120 [hep-ex] (cit. on pp. 7, 13).

[74] ATLAS Collaboration, *ATLAS flavour-tagging algorithms for the LHC Run 2 pp collision dataset*, Eur. Phys. J. C **83** (2023) 681, arXiv: 2211.16345 [physics.data-an] (cit. on p. 7).

[75] ATLAS Collaboration, *Calibration of the light-flavour jet mistagging efficiency of the b-tagging algorithms with Z+jets events using 139* fb^{-1} *of ATLAS proton-proton collision data at* $\sqrt{s}$ = 13 *TeV*, Eur. Phys J. C **83** (2023) 728, arXiv: 2301.06319 [hep-ex] (cit. on pp. 7, 13).

[76] ATLAS Collaboration, *Measurement of the c-jet mistagging efficiency in* $t\bar{t}$ *events using pp collision data at* $\sqrt{s}$ = 13 *TeV collected with the ATLAS detector*, Eur. Phys. J. C **82** (2021) 95, arXiv: 2109.10627 [hep-ex] (cit. on pp. 7, 13).

[77] ATLAS Collaboration, *Performance of missing transverse momentum reconstruction with the ATLAS detector using proton–proton collisions at* $\sqrt{s}$ = 13 *TeV*, Eur. Phys. J. C **78** (2018) 903, arXiv: 1802.08168 [hep-ex] (cit. on p. 7).

[78] ATLAS Collaboration, *Topological cell clustering in the ATLAS calorimeters and its performance in LHC Run 1*, Eur. Phys. J. C **77** (2017) 490, arXiv: 1603.02934 [hep-ex] (cit. on p. 7).

[79] D. Krohn, J. Thaler and L.-T. Wang, *Jet trimming*, JHEP **02** (2010) 084, arXiv: 0912.1342 [hep-ph] (cit. on p. 7).

[80] ATLAS Collaboration, *In situ calibration of large-radius jet energy and mass in* 13 *TeV proton–proton collisions with the ATLAS detector*, Eur. Phys. J. C **79** (2019) 135, arXiv: 1807.09477 [hep-ex] (cit. on pp. 7, 13).

[81] ATLAS Collaboration, *Measurement of the ATLAS Detector Jet Mass Response using Forward Folding with* $80\,fb^{-1}$ *of* $\sqrt{s} = 13$ *TeV pp data*, ATLAS-CONF-2020-022, 2020, URL: https://cds.cern.ch/record/2724442 (cit. on pp. 7, 13).

[82] ATLAS Collaboration, *Performance of top-quark and W-boson tagging with ATLAS in Run 2 of the LHC*, Eur. Phys. J. C **79** (2019) 375, arXiv: 1808.07858 [hep-ex] (cit. on pp. 7, 13).

[83] A. J. Larkoski, I. Moult and D. Neill, *Power counting to better jet observables*, JHEP **12** (2014) 009, arXiv: 1409:6298 [hep-ph] (cit. on p. 7).

[84] ATLAS Collaboration, *Boosted hadronic vector boson and top quark tagging with ATLAS using Run 2 data*, ATL-PHYS-PUB-2020-017, 2020, URL: https://cds.cern.ch/record/2724149 (cit. on pp. 7, 13).

[85] ATLAS Collaboration, *ATLAS simulation of boson plus jets processes in Run 2*, ATL-PHYS-PUB-2017-006, 2017, URL: https://cds.cern.ch/record/2261937 (cit. on p. 10).

[86] A. D. Martin, W. J. Stirling, R. S. Thorne and G. Watt, *Parton distributions for the LHC*, Eur. Phys. J. C **63** (2009) 189, arXiv: 0901.0002 [hep-ph] (cit. on p. 10).

[87] ATLAS Collaboration, *Measurement of the cross-section and charge asymmetry of W bosons produced in proton–proton collisions at* $\sqrt{s} = 8$ *TeV with the ATLAS detector*, Eur. Phys. J. C **79** (2019) 760, arXiv: 1904.05631 [hep-ex] (cit. on p. 10).

[88] ATLAS Collaboration, *Measurements of top-quark pair differential cross-sections in the* $e\mu$ *channel in* pp *collisions at* $\sqrt{s} = 13$ *TeV using the ATLAS detector*, Eur. Phys. J. C **77** (2017) 292, arXiv: 1612.05220 [hep-ex] (cit. on p. 10).

[89] ATLAS Collaboration, *Estimation of non-prompt and fake lepton backgrounds in final states with top quarks produced in proton-proton collisions at* $\sqrt{s} = 8$ *TeV with the ATLAS detector*, ATLAS-CONF-2014-058, 2014, URL: https://cds.cern.ch/record/1951336 (cit. on p. 12).

[90] ATLAS Collaboration, *Studies of* $t\bar{t}/tW$ *interference effects in* $b\bar{b}\ell^+\ell^{-\prime}\nu\bar{\nu}'$ *final states with* POWHEG *and* MADGRAPH5_AMC@NLO *setups*, ATL-PHYS-PUB-2021-042, 2021, URL: https://cds.cern.ch/record/2792254 (cit. on p. 13).

[91] J. Butterworth et al., *PDF4LHC recommendations for LHC Run II*, J. Phys. G **43** (2016) 023001, arXiv: 1510.03865 [hep-ph] (cit. on p. 13).

[92] ATLAS Collaboration, *Performance of pile-up mitigation techniques for jets in* pp *collisions at* $\sqrt{s} = 8$ *TeV using the ATLAS detector*, Eur. Phys. J. C **76** (2016) 581, arXiv: 1510.03823 [hep-ex] (cit. on p. 13).

[93] ATLAS Collaboration, E_T^{miss} *performance in the ATLAS detector using 2015–2016 LHC* pp *collisions*, ATLAS-CONF-2018-023, 2018, URL: https://cds.cern.ch/record/2625233 (cit. on p. 13).

[94] A. L. Read, *Presentation of search results: the* CL_s *technique*, J. Phys. G **28** (2002) 2693 (cit. on p. 14).

[95] T. Junk, *Confidence level computation for combining searches with small statistics*, Nucl. Instrum. Meth. A **434** (1999) 435, arXiv: hep-ex/9902006 (cit. on p. 14).

[96] G. Cowan, K. Cranmer, E. Gross and O. Vitells, *Asymptotic formulae for likelihood-based tests of new physics*, Eur. Phys. J. C **71** (2011) 1554, arXiv: 1007.1727 [physics.data-an], Erratum: Eur. Phys. J. C **73** (2013) 2501 (cit. on p. 14).

Appendix

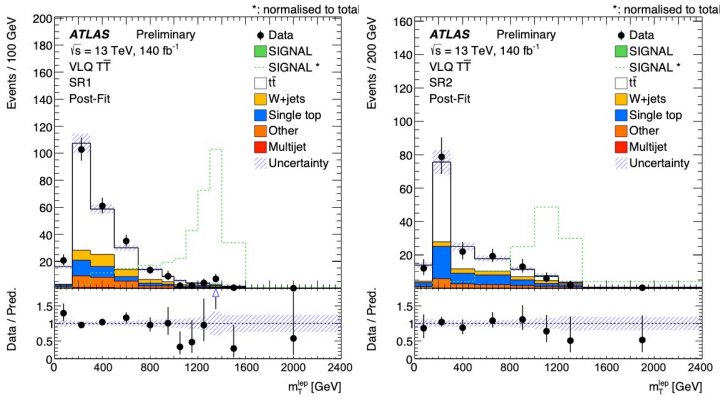

Figure 8: Distributions of m_T^{lep} in the two signal regions after the signal+background fit. The signal corresponds to $T\bar{T}$ with $m_{\text{VLQ}} = 1400\,\text{GeV}$ and $\mathcal{B}(T \to Wb) = 1$. The lower panels of each plot show the ratio of data to the fitted background yields. The band represents the systematic uncertainty after the maximum-likelihood fit. The dashed green histogram shows the shape of the signal scaled to the integral of the background.

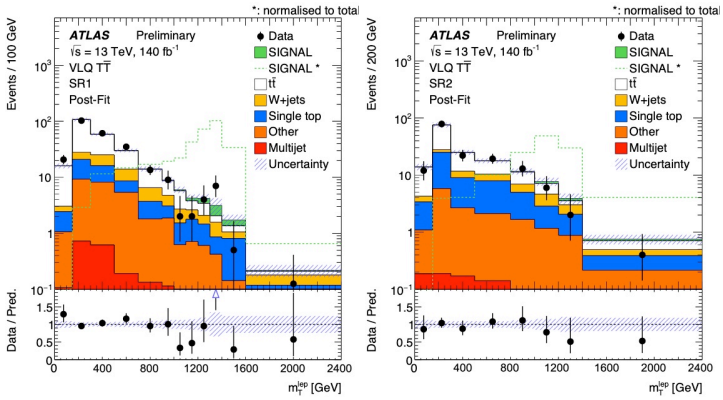

Figure 9: Log-scale distributions of m_T^{lep} in the two signal regions after the signal+background fit. The signal corresponds to $T\bar{T}$ with $m_{\text{VLQ}} = 1400\,\text{GeV}$ and $\mathcal{B}(T \to Wb) = 1$. The lower panels of each plot shows the ratio of data to the fitted background yields. The band represents the systematic uncertainty after the maximum-likelihood fit. The dashed green histogram shows the shape of the signal scaled to the integral of the background.

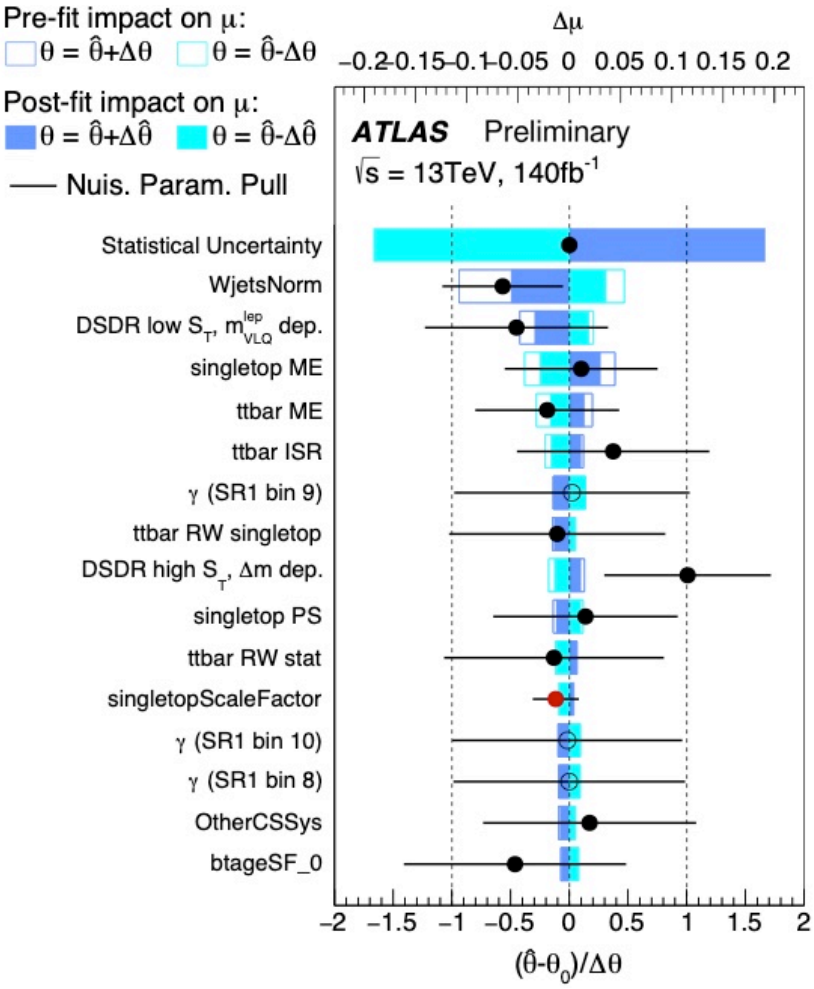

Figure 10: Ranking of uncertainties by their impact on the signal strength ($\Delta\mu$) for the signal+background fit for a signal with $m_{\mathrm{VLQ}} = 1400\,\mathrm{GeV}$ and $\mathcal{B}(T \to Wb) = 1$. Dark (light) blue boxes shows how much μ changes (top axis) when a fit is performed that has the given parameter fixed to a value that is shifted by $+1\sigma$ (-1σ) from its best-fit value. The open (filled) boxes correspond to shifting the parameter by its pre-fit (post-fit) uncertainty. The circles show the best-fit value of the given nuisance parameter relative to its pre-fit uncertainty (bottom axis). The circle style (red, open, or black) indicates the type of nuisance parameter (floated scale factor pull away from nominal, MC statistical uncertainty, or other). The black error bars shows the post-fit uncertainty relative to the pre-fit uncertainty, so unit width indicates no constraint due to the profile likelihood fit. Only the 15 highest ranked systematic uncertainties are shown.